Chapter 7

Strengthening bio-circularity by reinforcing waste-derived Triphasic calcium phosphate to fabricate Alumina toughened Zirconia biocomposite with enhanced bioactivity

7.1 Introduction

The current socioeconomic conditions of the developing world have presented significant challenges, such as ensuring food security, maintaining water quality and availability, mitigating global warming, managing limited energy resources, and promoting environmental conservation [1]. Unfortunately, many of the proposed solutions to these challenges can create further obstacles. For instance, food waste is a persistent issue that affects both food security and economic prosperity. One such source of food waste is animal waste bone (AWB), with estimations suggesting a staggering annual contribution of approximately 20 million metric tons globally [2]. This surplus stems from a diverse array of sources, such as slaughterhouses, eateries, and even everyday households. Efficiently handling this waste presents a formidable obstacle as it carries the risk of infectious disease transmission, compounded by the unpleasant odor accompanying direct ground disposal [3]. Furthermore, the improper disposal of such waste onto agriculturally productive and fertile land can lead to soil contamination and the impairment of land fertility [4]. Improperly managing the disposal of animal bone waste originating from restaurants and slaughterhouses not only incurs additional costs in terms of capital and resources for appropriate disposal [5] but also results in potential revenue loss. Conversely, harnessing the potential of these by-products in a resourceful manner can yield substantial economic benefits for a nation. Failing to address this waste mismanagement not only undermines environmental conservation but also hampers the pursuit of sustainable development goals.

In addition to traditional approaches, there is a growing interest in exploring alternative solutions that not only address these pressing issues but also generate economic benefits while minimizing waste [6]. The circular economy, or more specifically, the bioeconomy, has emerged as a promising approach advocated by global experts to tackle

these complex and interconnected problems [7]. The paradigm of biocircularity represents a holistic approach to the sustainable production of renewable biological materials, prioritizing their extended usage, optimal reuse, and recycling [8]. Researchers have delved into the exploration of animal waste bone (AWB) for diverse applications, capitalizing on its inherent composition, particularly hydroxyapatite (HAp). Simple transformation processes enable the conversion of HAp into tricalcium phosphate (TCP) [9]. The catalytic, thermal, and chemical stability exhibited by HAp make it an attractive candidate for biodiesel production [10-12]. AWB derived from different animal species possess varying elemental compositions, resulting in different catalytic properties. For instance, Khan et al. developed a low-cost biodiesel catalyst from ostrich waste bone. At the same time, Chingakham et al. synthesized a heterogeneous catalyst for biodiesel transesterification by calcining and hydrothermal reaction of AWB [13,14]. In a similar vein, Prabu et al. undertook the synthesis of a magnetic absorbent derived from lamb bone, showcasing its efficacy in the removal of heavy metals from aqueous solutions [15]. Amiri et al., on the other hand, harnessed ostrich waste bone to effectively eliminate cobalt from wastewater and activate peroxymonosulfate for dye degradation [16]. The versatility of AWB extends to its composition, as it serves as a rich source of essential amino acids, minerals, and vitamin B12, making it a suitable candidate for the preparation of animal feed products [17]. Moreover, Gendy et al. successfully synthesized a green nano-bio-catalyst, fluorapatite, from waste bone for the purpose of purifying wastewater generated by the petroleum industry [18].

However, the most profound AWB utilization comes from biomaterial production due to abundance of hydroxyapatite content [19]. Hydroxyapatite (HAp) is a critically important bioactive material found abundantly in natural hard tissues, such as bones and teeth, constituting approximately 70% of their structure [20]. Its remarkable

biocompatibility and bioactivity make HAp the most suitable ceramic material for prosthetic applications, including artificial bones and teeth [21-24]. Non-stoichiometric hydroxyapatite, obtained from diverse sources such as fish, bovine bones, eggshells, and chicken bones, has exhibited remarkable biological characteristics surpassing those achieved through synthetic means [25]. This superiority can be attributed to the presence of essential ions like Cl, F, K, Mg, Na, SO_4 and Sr, which contribute to advantageous properties facilitating accelerated bone regeneration [26]. Among these minor elements, magnesium (Mg) is present at a higher concentration, contributing to the formation of the Whitlockite phase [27,28]. The inorganic component of human bone consists predominantly of hydroxyapatite, with a secondary presence of whitlockite, in a ratio of 3:1 [29]. Heat treatment of animal bones can produce a composite material called HAp/TCP/Whitlockite, which possesses excellent biocompatibility, bioactivity, and osteoconduction properties [30]. However, high-temperature treatment induces the transformation of β-TCP into α-TCP, which is a less biocompatible material compared to β-TCP [31]. Nonetheless, in the presence of magnesium, the sintering process of TCP phases allows for higher densification. Furthermore, the presence of magnesium during the cooling process leads to a reversible transition from β to α, indicating that Mg^{2+} promotes the kinetics of α to β conversion upon cooling or slows down the kinetics of the β to α transition upon heating, thereby increasing the time required to reach equilibrium [32]. Emerging research has highlighted the enhanced bone healing potential of composite materials composed of hydroxyapatite combined with other calcium phosphate phases. These mixtures, specifically biphasic or biphasic/triphasic materials, have been shown to outperform single-phase materials in addressing defect areas and promoting effective bone regeneration [33,34].

Despite the advantages of calcium phosphate-based biocomposite, their

degradation caused by rapid revascularization has been observed, resulting in weakened pore structures that are unsuitable for load-bearing applications [35]. Consequently, the development of mechanically robust scaffolds based on calcium phosphate is of utmost importance in order to replicate the properties exhibited by natural bone [36]. To achieve this, the mechanical properties, particularly the strength and fracture toughness, of such composites need improvement. One such approach is the intrusion of either high-strength material into Calcium phosphate composites or doping of calcium phosphate into high-strength composites. Ceramic materials such as zirconia and alumina have emerged as excellent biomaterials, overcoming the limitations of calcium phosphate with their higher strength and improved mechanical properties [37,38]. Alumina exhibits excellent biocompatibility and mechanical strength, making it suitable for load-bearing implants and orthopedic devices. However, its brittleness can be a disadvantage, potentially leading to fractures under high stress [39]. Zirconia, on the other hand, demonstrates exceptional biocompatibility, mechanical properties, and resistance to wear and corrosion. Both alumina and zirconia have certain drawbacks: alumina is hard to machine and prone to brittleness, while zirconia can be difficult to sinter and undergoes a phase transformation at high temperatures, causing weakness [40]. To address these limitations, alumina toughened zirconia (ATZ) has been developed as a composite material. ATZ combines the properties of alumina and zirconia by dispersing alumina particles in a zirconia matrix. This composite enhances resistance to crack propagation, reducing the risk of catastrophic failure. ATZ offers improved toughness and reliability compared to pure alumina or zirconia [41]. Consequently, ATZ has gained popularity in biomedical applications, including dental crowns, bridges, implants, artificial joints, and bone plates, where higher toughness and reliability are required [42-43].

The objective of the present research is to advance the principles of biocircularity

in biomaterial production by incorporating waste-derived calcium phosphate phases into an alumina toughened zirconia (ATZ) composite, resulting in the development of a HAp/TCP/Wk-ATZ biocomposite. This fabricated composite is designed to possess improved bioactivity while maintaining its mechanical properties. By incorporating animal waste bone (AWB) into the ATZ composite, the bioactivity of the material can be enhanced, promoting stronger bonds with surrounding bone tissues. HAp/TCP/Wk, which constitutes the primary inorganic component of natural bone, exhibits exceptional bioactivity, fostering the formation of a bioactive interface with adjacent bone tissue. This facilitates superior osseointegration, bolstering the long-term stability and performance of the implant. Additionally, the utilization of waste-based dopants and cost-effective materials like alumina provides an avenue for fabricating a low-cost zirconia-based biocomposite with enhanced bioactivity.

7.2 Materials and Methodology

7.2.1 Raw materials

The basic raw materials used to fabricate AWB-doped ATZ bio-composites are Zirconia, Alumina, and animal waste bone (AWB). Zirconia powder with an average grain size of 20 nm was purchased from Merck (Germany). The high-purity alumina powder used in this study was obtained from ALCOA ACC, CT 3000SG, located in Mumbai, Maharashtra, India. ATZ powder was prepared by mixing alumina and zirconia in a weight ratio of Alumina: Zirconia: 4:1 and then kept for pot milling for 24 hours. The AWB used in the study was sourced from leftover bone waste obtained from restaurants and butcher shops. To ensure the removal of unwanted substances like bone marrow and spices, the waste bone underwent a thorough washing process employing deionized water. Subsequently, the washed bone was subjected to a two-hour degreasing process by boiling it with common salt. After degreasing, the bone was dried, and it was crushed in an oven and grinder,

respectively. The bone powder was then thermally treated at a temperature of 1000°C and milled using a rotary mill equipped with iron blades. The resulting powder was sieved to obtain particles smaller than 150 µm using appropriate sieves.

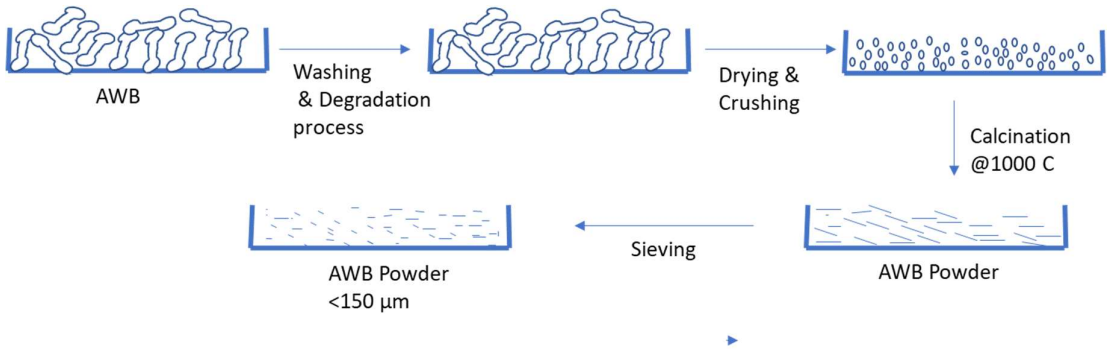

Figure .7.1. AWB Processing way step by step.

7.2.2 Fabrication of AWB-ATZ Biocomposite

The fabrication of AWB-ATZ composite involves preparing various composition mixtures of AWB in ATZ with varying AWB wt%. Four composition mixtures were prepared by varying AWB wt% (5, 10, 15, 20). Up to 20 wt % of AWB is incorporated into ATZ. This mixture composition is further added with a suitable binder (Sucrose solution with Sucrose: Distilled Water::1:1), and then rectangular samples of size 40 by 10 by 10 were prepared using a Hydraulic press with a 10-ton load. These samples are then kept for thermal treatment at temperatures 1400°C and 1500°C.

Figure.7.2. Fabrication of AWB-ATZ processing sequence.

7.2.3 Characterization Technique

The apparent porosity of the sintered AWB-ATZ biocomposite was determined using the water immersion technique, which is based on Archimedes' principle. Fourier Transform Infrared (FTIR) spectroscopy was used to identify the functional groups and phases existing in the sintered samples. This characterization was conducted using a BRUKER (Yokohama, Kanagawa, Japan) TENSOR 27–3772 instrument. X-ray diffraction (XRD) analysis was also performed to examine the crystalline phases present in the samples. Surface morphology of the developed AWB-ATZ biocomposite was studied using Scanning Electron Microscopy (SEM) with an FEI Inspect S30 (Sweden) instrument. At the same time, High-Resolution Transmission Electron Microscopy (HRTEM) analysis was conducted using an FEI TECNAI G2-20 TWIN (Eindhoven, Netherlands) instrument to obtain detailed images of the material's structure at high resolution. Energy Dispersive X-ray spectroscopy (EDS) was employed to determine the elemental compositions of all the samples. The bioactivity of the doped and undoped samples was evaluated by immersing the materials in a modified simulated body fluid (1.5×SBF). The 1.5×SBF was prepared with an ion concentration 1.5 times higher than that of standard simulated body

fluid (SBF), as proposed by Kokubo and Takadama. The pH of the 1.5×SBF was adjusted to 7.4 using HCl and Tris-hydroxymethyl-aminomethane. Each sample was immersed in 40 ml of 1.5×SBF and maintained at a constant temperature of 36.5°C for 2 and 4 weeks. The bioactivity of the samples was assessed by observing the presence of a layer with a typical Ca/P ratio of apatite-like forms using SEM and EDS analysis.

7.3 Results and Discussion

Table. 7.1. XRF analysis of AWB powder**.**

S.NO.	COMPOUNDS	Wt %
1	SiO_2 (%)	1.97
2	TiO_2	ND
3	Al2O3	0.58
4	MnO	ND
5	Fe_2O_3	0.06
6	CaO	56.33
7	MgO	1.35
8	Na_2O	1.22
9	K_2O	0.22
10	P_2O_5	37.32
11	V_2O_5	ND
12	Cr_2O_3	ND
13	CuO	ND
14	ZnO	0.02
15	ZrO_2	ND
16	BaO	ND
17	H_2O	0.50
18	Total	99.57

7.3.1 Characterization of raw AWB

Various characterization techniques have been employed to study the raw materials' physicochemical characteristics for preparing bio-composites. The XRF analysis of powder

obtained after physical, chemical, and mechanical treatment of AWB reveals that AWB powder primarily consists of oxides of Calcium and phosphorus, with a lesser amount of magnesium oxides (Table 7.1). Additionally, X-ray diffraction (XRD) analysis confirmed the presence of calcium and phosphorus elements in the raw AWB by identifying the existence of monocrystalline apatite in the bone matrix, and the diffraction peaks matched the characteristic pattern of hydroxyapatite (HAp) (JCPDS No. 72-1243). The presence of wide and short diffraction peaks indicates the low crystallinity and small grain size of HAp (Fig. 7.3 (a)). The thermal degradation behavior of AWB was investigated using thermogravimetric analysis (TGA), and the results are depicted in Figure 7.3 (b). The degradation process of AWB can be observed to occur in three distinct stages. Initially, there is the evaporation of entrapped water, which takes place between room temperature and 150°C. Subsequently, the organic material, primarily collagen, undergoes decomposition in the temperature range of 200°C to 600°C. Finally, in the temperature range of 600°C to 1000°C, the structural carbonate decomposes, resulting in the release of carbon dioxide. Approximately 35% of the total weight loss was observed during the degradation process, with the remaining 65% comprising burnt-out residue. Similar findings were also reported by Mayank et al. [2]. These observations indicate that all the organic constituents of the raw bone are eliminated during the heat treatment process.

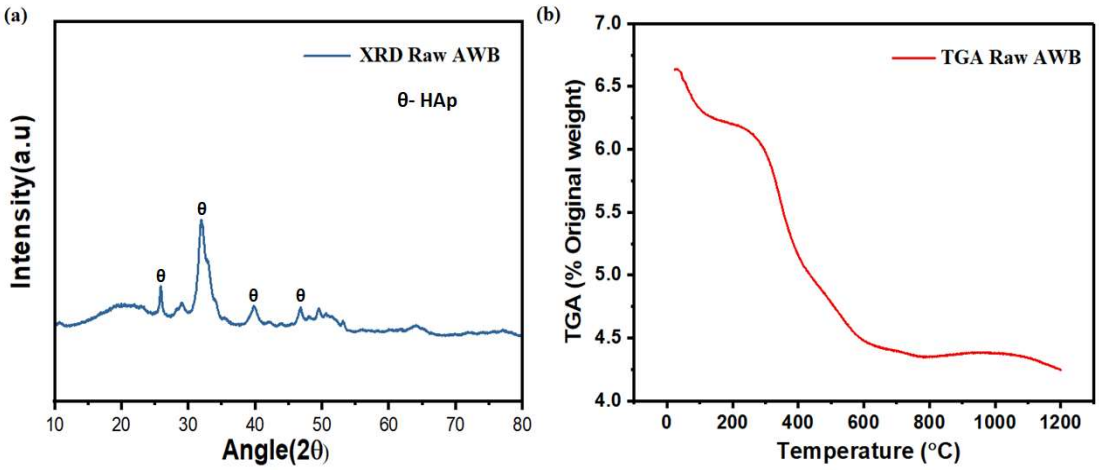

Figure. 7.3. (a)- XRD of raw AWB, (b)- TGA of raw AWB.

7.3.2 Characterizations of developed AWB-ATZ biocomposite

The X-ray diffraction (XRD) patterns were used to determine the presence of different phases and their conversion in the composite (ATZ-AWB) resulting from the addition of AWB and high-temperature sintering. XRD analysis of pure ZTA samples sintered at 1400°C and 1500°C revealed the presence of zirconia and alumina in various phases (Fig. 7.3 and 7.4). Zirconia was predominantly found in the tetragonal form, along with some monoclinic phases, while alumina existed as α-Alumina due to the high-temperature sintering process. The tetragonal phase of ZrO_2 was more prominent, with weaker peaks originating from the monoclinic phase of ZrO_2. The coexistence of both monoclinic and tetragonal phases is attributed to the partial conversion of monoclinic ZrO_2 to tetragonal ZrO_2 facilitated by the presence of 3 mol% yttria. These findings align with previously reported results. On the other hand, sintering pure AWB samples at temperatures of 1400°C and 1500°C revealed the presence of Hydroxyapatite (HAp), Tricalcium phosphate (TCP), and Whitlockite (Wk) phases. At higher sintering temperatures, HAp underwent decomposition and transformed into the β-TCP phase. Additionally, β-TCP also transformed, forming the high-temperature phase of TCP known as α-TCP. At both

sintering temperatures, all three phases (HAP, β-TCP, and α-TCP) are significant, indicating incomplete formation of HAP to β-TCP and β-TCP to α-TCP. The decomposition of HAP is relatively consistent with increasing sintering temperature, while the conversion of β-TCP to α-TCP becomes more pronounced, resulting in higher α-TCP content. Additionally, Whitlockite, a form of calcium phosphate that forms in the presence of magnesium ions, is present. Since animal bone was used as a substitute for HAp doping, the minor amount of magnesium present in the raw bone leads to the transformation of Whitlockite along with β-TCP from HAp during high-temperature sintering.

Table. 7.2 Semiquantitative Analysis (%) of AWB-ATZ biocomposite using XpertHigh Score.

S. No.	Hydroxyapatite (HAp)	β-TCP	α-TCP	Whitlockite (Wk)	α-Alumina	*m*-ZrO_2	*t*-ZrO_2	*c*-ZrO_2	Calcium Zirconium Oxide	Calcium Zirconium Oxide
Formula	$Ca_{10}(PO_4)_6(OH)_2$	$Ca_3(PO_4)_2$	$Ca_3(PO_4)_2$	$Ca_{18}Mg_2H_2(PO_4)_{14}$	Al2O3	ZrO_2	ZrO_2	ZrO_2	$Ca_{0.15}Zr_{0.85}O_{1.85}$	$CaZrO_3$
Reference Code (JCPD no.)	74-0566	70-2065	70-0365	70-2064	71-1683	83-0944	79-1763	81-1550	26-0341	75-0358
Crystal Structure	Hexagonal	Rhombohedral	Monoclinic	Rhombohedral	Rhombohedral	Monoclinic	Tetragonal	Cubic	Cubic	Cubic
AWB-1400°C	41	35	13	12						
AWB-1500°C	41	38	16	5						
ATZ-1400°C					22	38	40			
ATZ-1500°C					20	40	40			
ATZ-AWB-5%-1400°C	1	2	1	1	19	39	37			
ATZ-AWB-5%-1500°C	1	2	1	1	20	38	37			
ATZ-AWB-10%-1400°C	2	4	2	2	21	27	34	5	3	
ATZ-AWB-10%-1500°C	2	4	2	2	20	24	35	5	6	
ATZ-AWB-15%-1400°C	4	5	3	3	20	20	33	5	5	2
ATZ-AWB-15%-1500°C	4	5	3	3	20	19	34	5	4	3
ATZ-AWB-20%-1400°C	5	6	5	4	20	17	27	6	7	3
ATZ-AWB-20%-1500°C	5	6	5	4	20	13	26	7	11	3

When ATZ samples are doped with AWB-derived HAp powders and sintered at higher temperatures, the dominant phases are zirconia due to the higher zirconia content (more than 64 wt%). The second most abundant phase is α-Alumina (more than 16 wt%), while the peaks of HAp, TCP, and Whitlockite are relatively smaller due to their lower abundance in the composite. Interestingly, the appearance of cubic-zirconia, a third phase of Zirconia, is also observed when ATZ is doped with AWB and sintered at 1400°C. This can be attributed to the reaction between ZrO_2 and HAp, leading to the decomposition of HAp into TCP and Calcium oxide (CaO). The excess CaO dissolves completely in the ZrO_2 phases,

transforming them into tetragonal and cubic phases. The decomposition of AWB in the presence of Zirconia at higher temperatures also results in the formation of stoichiometric and non-stoichiometric forms of $CaZrO_3$. These forms are more evident at higher AWB concentrations, preferably greater than 15 wt%, and higher sintering temperatures (1500°C). The formation of $CaZrO_3$ may be attributed to the reaction of Zirconia with the remaining CaO, which was present after the intrusion into Zirconia and its transformation into cubic and tetragonal forms. High-temperature sintering promotes the formation of $CaZrO_3$. In addition to α-Alumina and Zirconia phases (*m, t, c*-ZrO_2), the presence of Calcium phosphate in the forms of HAP, TCP (β-TCP and α-TCP), and Whitlockite is also evident. The content of these Calcium phosphate forms increases with an increase in the weight percentage of AWB in the ATZ composite. High-temperature sintering, specifically from 1400°C to 1500°C, enhances the α-TCP and $CaZrO_3$ content [44,45]. Xpert high score software quantifies phase formation in AWB-doped ATZ samples after sintering (Table 7.2).

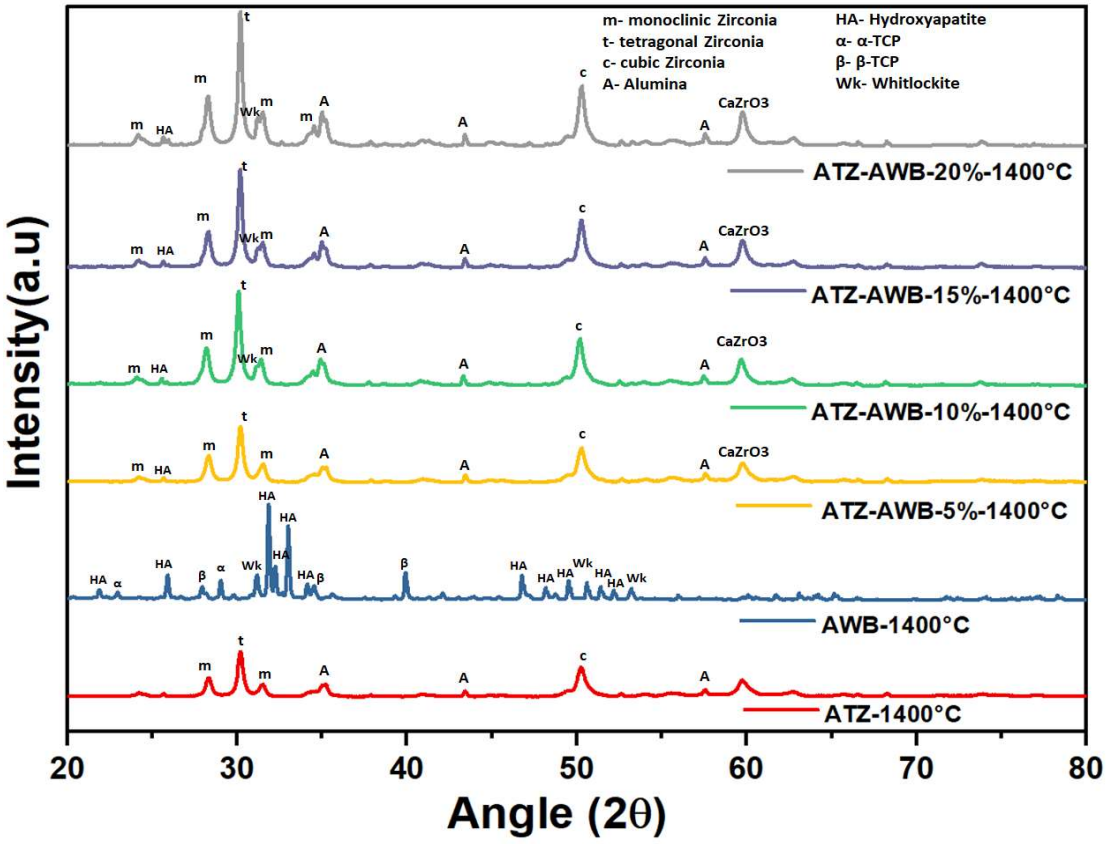

Figure. 7.4. XRD pattern of AWB-ATZ biocomposite sintered at 1400°C.

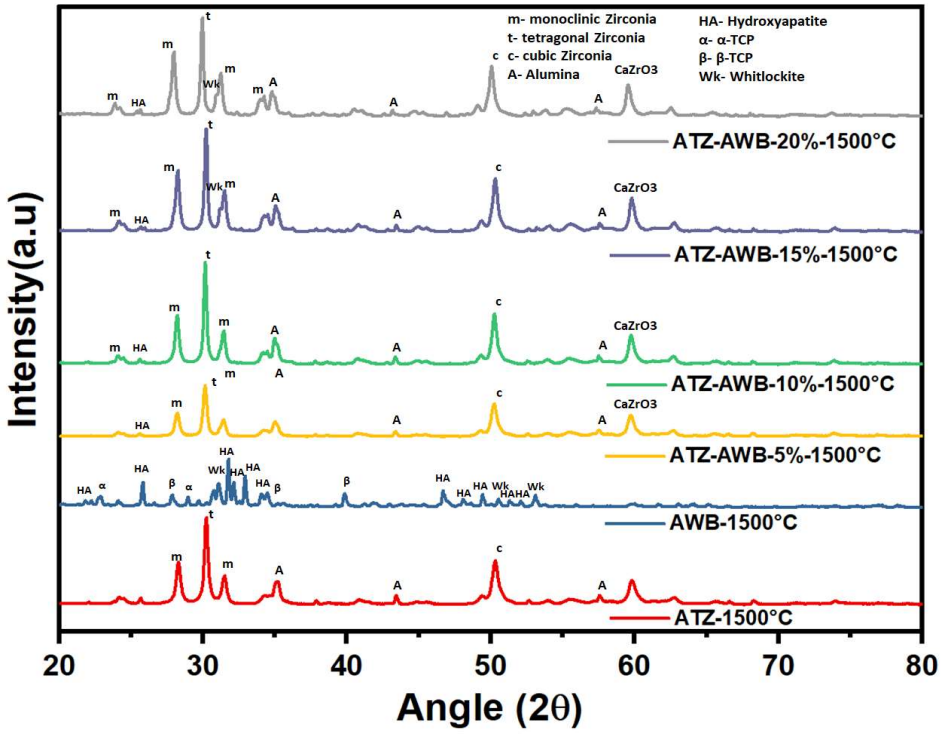

Figure. 7.5. XRD pattern of AWB-ATZ biocomposite sintered at 1500°C.

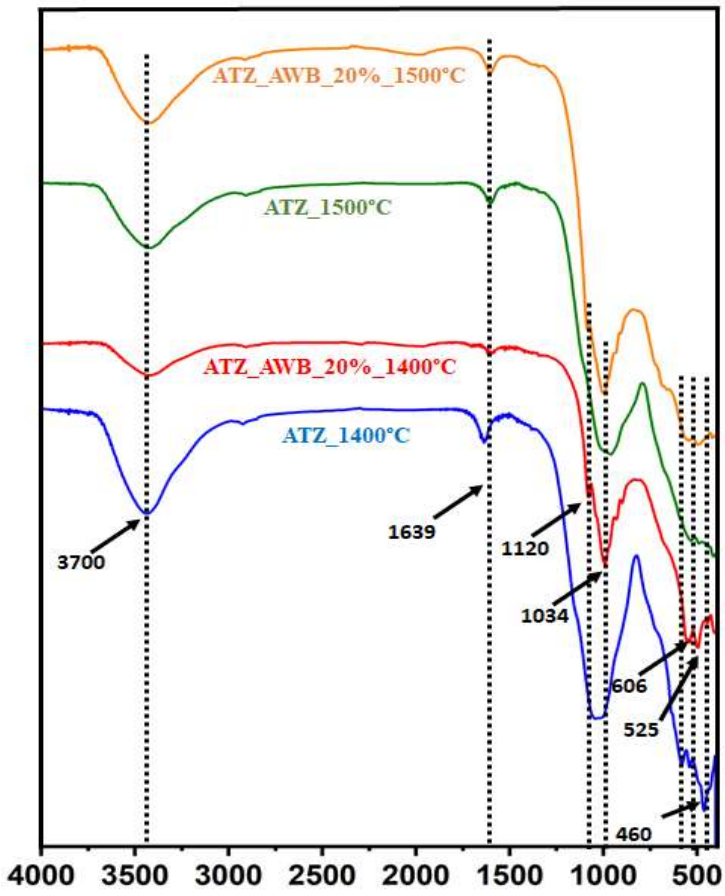

Figure. 7.6. FTIR pattern of AWB-ATZ biocomposite sintered at 1400°C and 1500°C.

The FTIR results were analyzed to confirm the coexistence of triphasic calcium phosphate (HAp, TCP, and Wk) with ATZ. The FTIR peaks for pure ATZ samples sintered at 1400°C and 1500°C are shown in Figure 7.6, clearly indicating the presence of zirconia and alumina in the composite. In the FTIR spectra, absorption bands in the range of 1600-1650 cm^{-1} and 3000-3700 cm^{-1} were observed, which can be assigned to the O-H vibration mode. These bands correspond to the bending and stretching vibrations of the O-H bond due to absorbed water. The absorption peaks at 460 cm^{-1} and 540 cm^{-1} are attributed to the stretching vibrational modes of Zr-O and Zr-O-Zr, respectively. Similarly, the bands around 450 cm^{-1} and 525 cm^{-1} are associated with the stretching vibrations of Al-O bonds. The broad absorption in the range of 950-1200 cm^{-1} indicates the formation of Al-O-Al

bonds. Specific peaks related to alumina are observed at 1400 cm^{-1}, 1034 cm^{-1}, and 563 cm^{-1}. With the addition of AWB, additional peaks appear in conjunction with alumina and zirconia. Figure 4 depict the FTIR spectra of AWB-doped ATZ samples sintered at 1400°C and 1500°C. A peak at 1029 cm^{-1} represents the v_3 phosphate group (PO_4^{3-}). Peaks at 963 cm^{-1} and 606 cm^{-1} can be attributed to the stretching vibration (υ_1) and bending vibration (υ_4) of the O-P-O bond in the phosphate (PO_4^{3-}) group. The asymmetric stretching band of the (PO_4^{3-}) group can be observed at 1120 cm^{-1}. These peaks are characteristic of various calcium phosphate structures, thus confirming the presence of HAp and TCP. The peak at 872 cm^{-1} corresponds to the HPO_4^{2-} group, confirming the existence of Wk [46-48]. The simultaneous presence of HAp, TCP, and Wk makes it challenging to distinguish individual peaks corresponding to a specific phase.

7.3.3 Microstructural characterizations of Animal Waste Bone-Alumina toughened zirconia (AWB-ATZ) biocomposite

Further, to have a better understanding of the structure of fabricated ATZ and AWB-doped ATZ biocomposite, microstructural analysis using HR-TEM and SEM is done. Fig.7.7 (a) shows an SEM image of ATZ sintered at 1400°C, showing partially developed grains of zirconia and alumina. The small and fine grains having the light color of Zirconia also confirmed through EDX analysis, are uniformly distributed over the entire surface range. The dark-coloured and large grains, approximately spherical in shape, are attributed to Alumina, also confirmed through EDX analysis. Further, when the ATZ sample is treated at 1500°C, the grains of both alumina and zirconia are fully developed, showing clear and fine grain boundaries, as clearly visible in the SEM image (Fig. 7.7 (b)). Zirconia grains are mostly spherical in shape, while alumina grains are distributed evenly and are irregularly shaped. When ATZ is doped with AWB and sintered at 1400°C, no interpretations can be drawn by visualizing SEM images (Fig. 7 .7c, d, e, f). However, a

significant effect in grain shape, size, and distribution over the entire surface is seen for the sample sintered at 1500°C, as evident from SEM images. The appearance of hexagonal and rhombohedron shapes in SEM images with an increase in AWB content and sintering to 1500°C is an indication of the formation of HAp, TCP, and Whitlockite. The alumina and zirconia grains remained unaltered and bore similar shapes, sizes, and patterns as undoped ATZ grains.

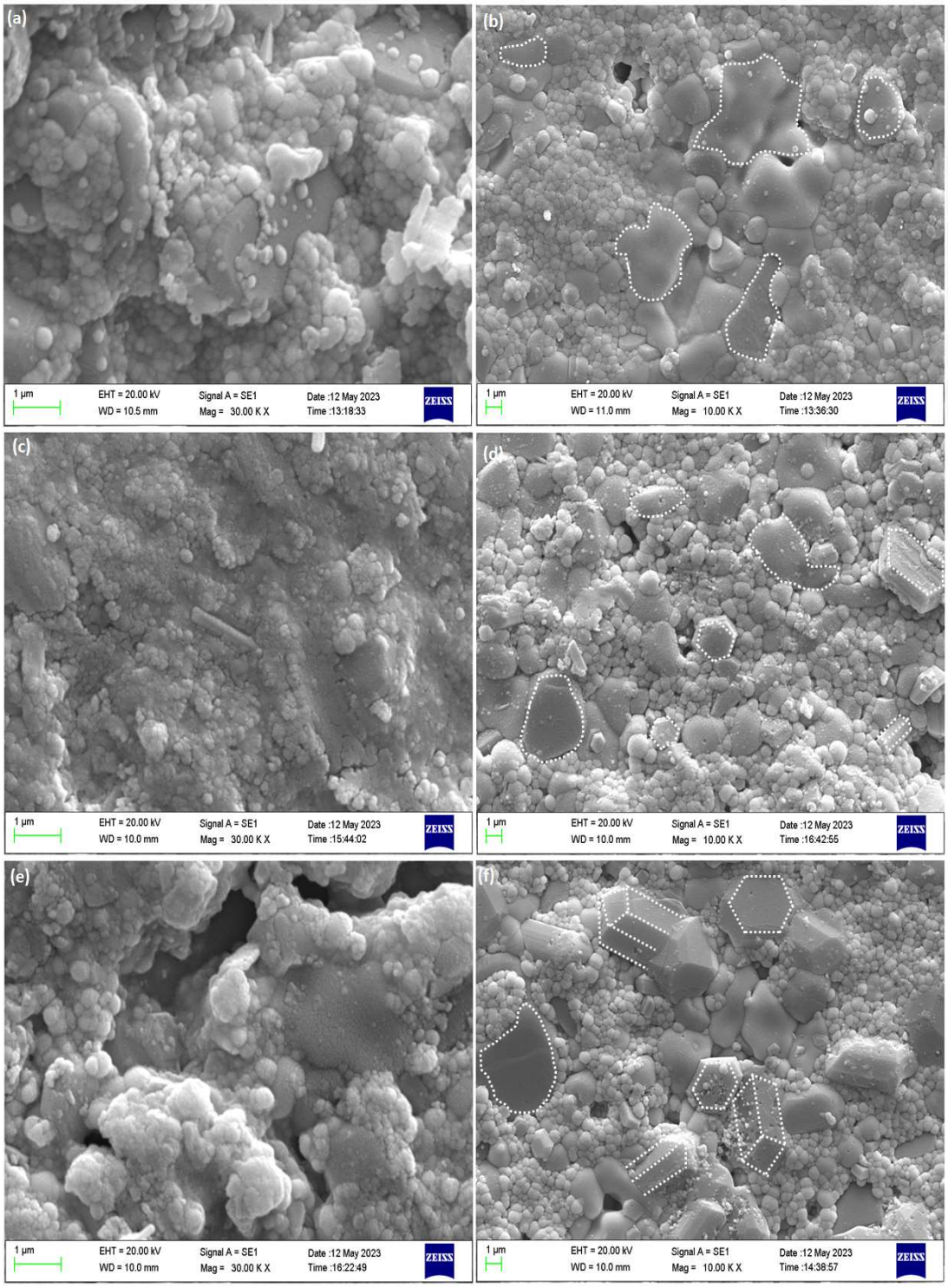

Figure. 7.7. Scanning Electron Microscope (SEM) of Animal Waste Bone-Alumina Toughened Zirconia (AWB-ATZ) biocomposites sintered at 1400°C and 1500°C. Zirconia grains are mostly spherical, alumina grains are distributed evenly, and are irregularly shaped. (a) shows an SEM image of ATZ sintered at 1400°C (b) ATZ sample is treated at 1500°C (c) shows an SEM image of ATZ-AWB5% sintered at 1400°C (d) ATZ-AWB-5% sample is treated at 1500°C (e) shows an SEM image of ATZ-AWB-10% sintered at 1400°C (f) ATZ-AWB10% sample is treated at 1500°C

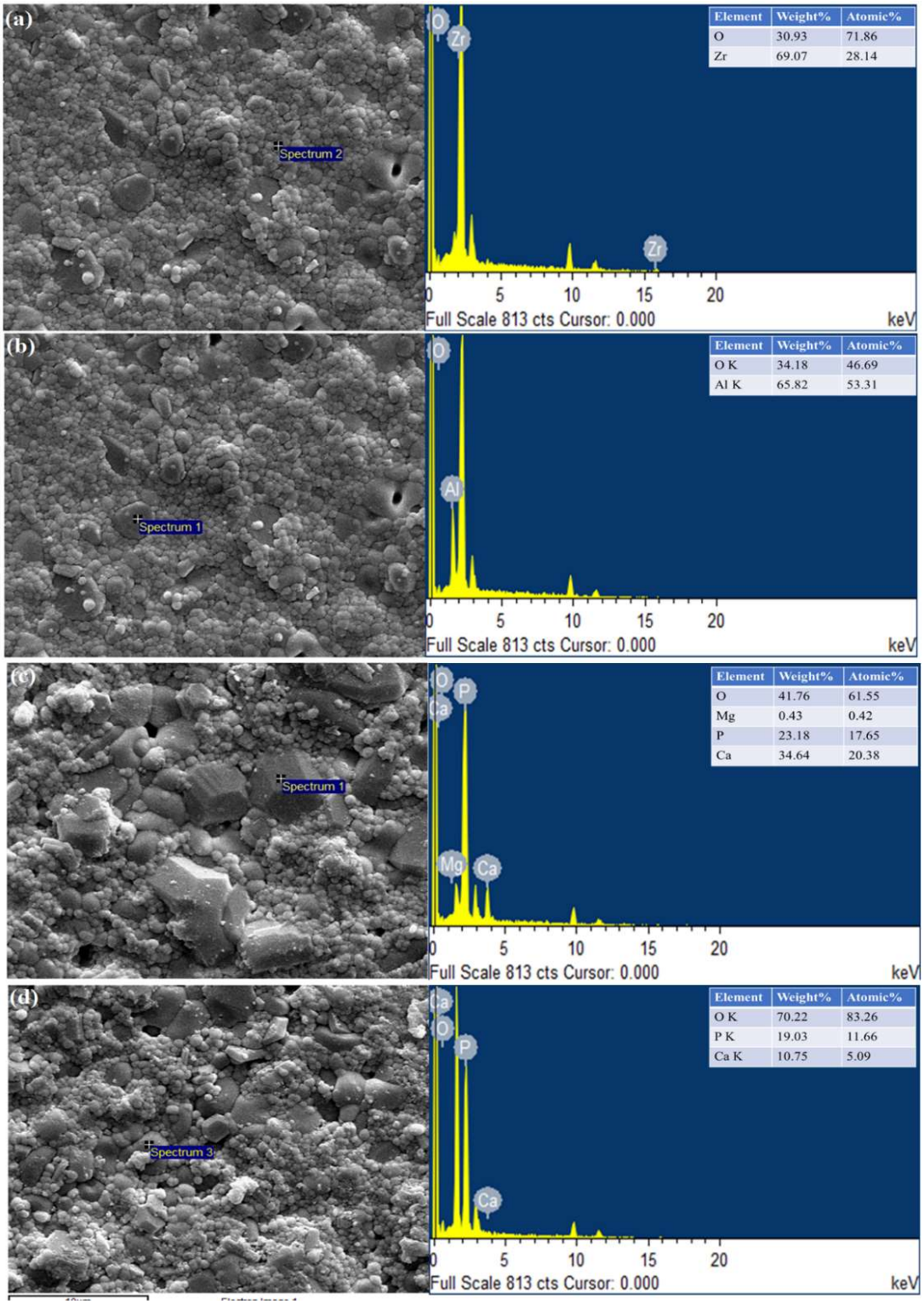

Figure. 7.8 Scanning Electron Microscope (SEM) with Energy-Dispersive X-ray Spectroscopy (EDS) of AWB-ATZ biocomposite sintered at 1500°C. The small and fine grains have the light color of Zirconia. The dark-coloured and large grains, approximately spherical in shape, are attributed to Alumina, confirmed through EDX analysis

Further analysis using Energy-Dispersive X-ray Spectroscopy (EDS) was conducted to investigate the elemental composition of AWB-ATZ composites, focusing on different particle shapes and their correlation with Scanning Electron Microscopy (SEM) analysis. The SEM images revealed the presence of small spherical particles, which were confirmed to be composed of Zirconia based on EDS analysis, indicating the presence of Zirconia and oxygen elements (fig. 7.8 (a)). Additionally, the larger irregular-shaped particles observed in the SEM analysis were identified as Alumina, as evidenced by the presence of Al and O atoms, thus supporting the SEM findings (fig. 7.8 (b)). The rhombohedral-shaped particles exhibited the presence of Mg, Ca, P, and O atoms, confirming the formation of the Whitlockite phase within the AWB-ATZ biocomposite (fig. 7.8 (c)). Finally, the hexagonal-shaped particle was determined to be either Hydroxyapatite (HAp) or Tricalcium Phosphate (TCP) since only Ca, P, and O atoms were detected during the EDS analysis (fig. 7.8 (d)). Overall, the EDS analysis provides strong evidence for the formation of HAp/TCP, Whitlockite, Alumina, and Zirconia phases within the developed AWB-ATZ biocomposite.

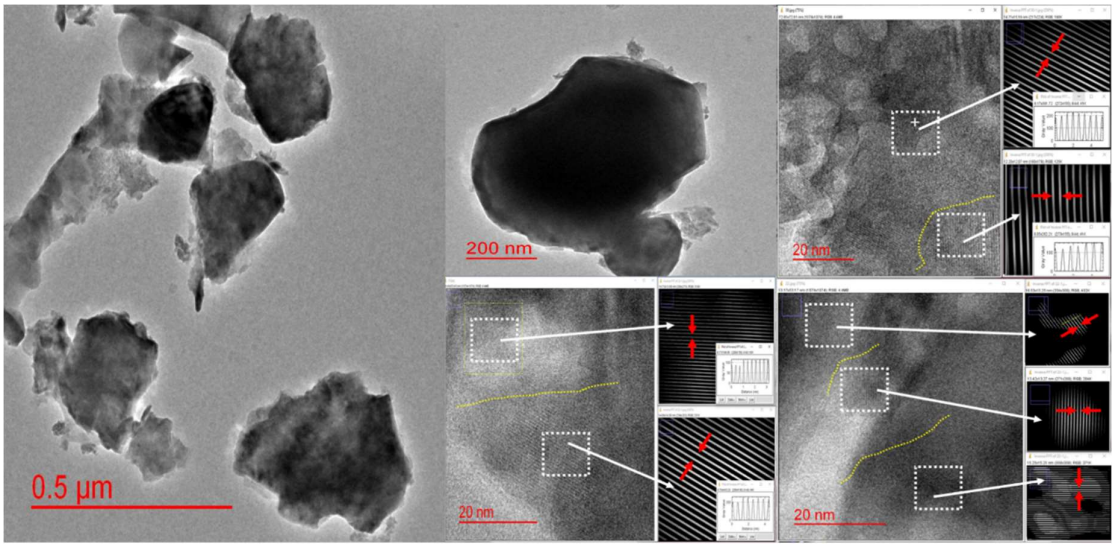

Figure. 7.9. Transmission electron microscope (TEM) of Alumina Toughened Zirconia-Animal Waste Bone (ATZ-AWB) biocomposites sintered at 1500°C.

Figure 7.9 presents high-resolution Transmission Electron Microscopy (TEM) images, providing a more detailed description of the geometric forms and morphology of the sample. The TEM micrograph reveals the presence of irregularly shaped crystals, which can be attributed to the presence of alumina and zirconia. Notably, a higher magnification TEM image exhibits a distinct hexagonal pattern, providing strong evidence for the presence of Hydroxyapatite (HAp). To further support these findings, the interplanar spacing of various crystals was determined using Image-J software on the HRTEM images. The results align closely with the expected lattice spacing of specific crystal planes in t-ZrO_2, α-Al2O3, HAp, β-TCP, and Wk. Specifically, the measured interplanar spacing values for the (101), (012), (101), (012), and (104) planes in these crystal structures were found to be 2.95473, 3.47732, 5.25985, 8.13816, and 6.44415, respectively. These observations provide further evidence for the presence and consistent characteristics of Zirconia, Alumina, HAp, and TCP/Wk within the sample.

7.3.4 Bioactivity, pH Analysis, and Biocorrosion Tests

The effect of zirconia bio-composites on the pH of the simulated body fluid (SBF) solution can be influenced by various factors, including the composition of the bio-composite, the immersion time, and the initial pH of the SBF solution. Figure 8 illustrates the pH changes of the sintered biocomposite samples during immersion in SBF for up to 28 days. The initial pH of the SBF solution was maintained at 7.40 for all samples. In the case of undoped ATZ biocomposite, the pH remains relatively unchanged due to the bio-inert nature of zirconia and alumina. However, a slight decreasing trend in the pH value is observed over time, which may be attributed to the release of aluminum ions into the SBF solution. The presence of aluminum ions can lead to a decrease in pH due to the formation of aluminum hydroxide. Moreover, ATZ samples sintered at higher temperatures exhibit a relatively lesser decrease in pH value compared to those sintered at lower temperatures, indicating a

lower release of aluminum ions. With the incorporation of HAp into ATZ, there is an enhanced release of calcium and phosphate ions into the SBF solution, resulting in an increase in pH due to the formation of calcium phosphate. Initially, at lower HAp concentrations in ATZ, the rate of increase in pH value is slow due to the diffusion of calcium ions from the HAp to the zirconia grains, which hinders the release of calcium ions. Additionally, the formation of β-TCP (tricalcium phosphate) due to the decomposition of HAp leads to a lower release of calcium and phosphate ions into the SBF solution, resulting in a slower rate of pH increase. As the HAp concentration in ATZ increases, there is a greater conversion of β-TCP, leading to improved release of calcium and phosphate ions into the SBF solution and a higher rate of pH increase. However, after around 5 days of immersion, the rate of pH increase due to the addition of HAp slows down. This can be attributed to the formation of an apatite layer on the sample surface, which contains phosphorus and calcium and hinders the further release of these ions, thereby decreasing the rate of pH increase. Furthermore, as the immersion time continues to increase, the pH of the SBF solution reaches a relatively constant level, indicating a steady state of ion release and pH balance.

The surfaces of the composites underwent in vitro bioactivity tests to assess their capacity to stimulate apatite formation. The composites were immersed in a simulated body fluid (SBF) solution for a duration of up to two weeks. The morphology of the scaffold surfaces underwent changes upon soaking in SBF. As early as the first week, apatite layers were observed to form on all samples, with each scaffold surface exhibiting a certain degree of white apatite deposition. After seven days of immersion, the pure ATZ composite (sintered at 1300 °C) displayed minimal apatite crystal growth on its surface. Energy-dispersive X-ray spectroscopy (EDX) analysis of these crystals confirmed the presence of calcium (Ca), phosphorus (P), and oxygen (O) elements, thus verifying the formation of

apatite. In contrast, the addition of AWB to ATZ resulted in densely populated apatite crystal deposition, indicating enhanced nucleation and growth rates of apatite due to the AWB addition. Increasing the immersion time in SBF from 7 to 14 days led to an expected increase in the size and quantity of the apatite layer. Notably, the growth of the apatite layer was significantly higher in AWB-doped samples compared to pure ATZ samples. These layers resembled a continuous arrangement of petal-like structures dispersed over the surface of the Animal Waste Bone-Alumina toughened zirconia (ATZ-AWB) composite. The apatite on the surface of ATZ composites appeared mostly as small-area fragments, while the AWB-added ATZ exhibited continuous growth akin to densely populated petals.

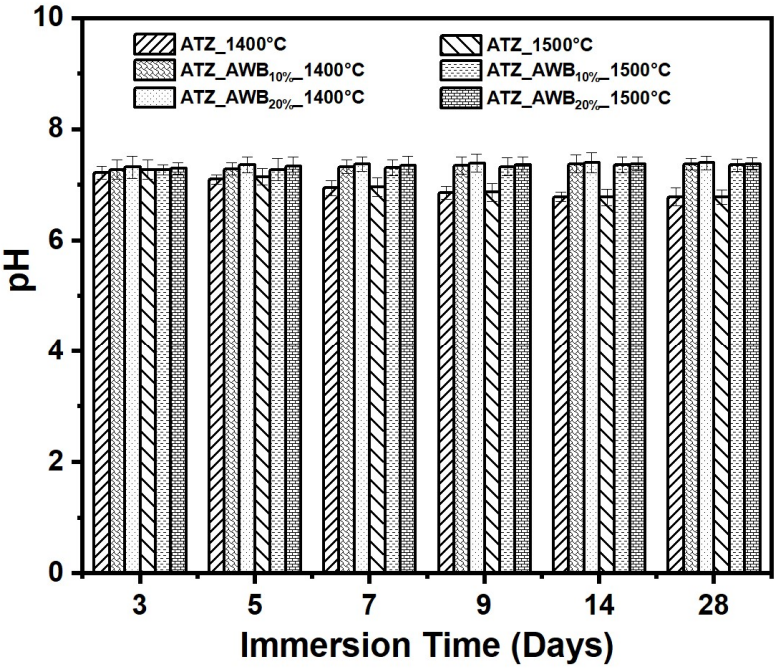

Figure. 7.10. pH variation of SBF solution after immersion of Animal Waste Bone-Alumina toughened zirconia (AWB-ATZ) biocomposite.

Furthermore, SEM images revealed that AWB-doped samples exhibited greater bioactivity compared to pure ATZ, with increasing AWB content in the ATZ-AWB composites correlating to higher material bioactivity (Fig.7.10). This can be attributed primarily to the formation of hydroxyapatite (HAp), tricalcium phosphate (TCP), and Whitlockite

(Whitlockite) through AWB. When the ATZ-AWB composite was immersed in an SBF solution, the calcium (Ca) and phosphate (PO_4) ions in the solution interacted with the HAp, TCP, and Whitlockite grains of the composite. The surface of HAp, TCP, and Whitlockite readily dissolved, releasing Ca and PO_4 ions into the solution. The high affinity of hydroxyapatite for these ions facilitated their adsorption onto the material's surface. As adsorbed Ca and PO_4 ions accumulated on the HAp, TCP, and Whitlockite surface, they formed small clusters or nuclei, serving as the initial building blocks for forming an apatite layer. These nuclei gradually grew and crystallized, resulting in the development of larger apatite crystals on the hydroxyapatite surface. The continuous supply of Ca and PO_4 ions from the SBF solution drove the process of crystal growth, with these ions incorporated into the growing crystals. Over time, the crystals grew and merged, forming a dense and continuous layer of apatite on the surface of the ATZ-AWB composite. This newly formed apatite layer closely resembled the mineral phase found in natural bone tissue. The presence of dense apatite layers can enhance the properties of osteointegration and osteoconduction. This bioactivity test confirms that the addition of AWB increases the bioactivity of the ATZ composite through the formation of a triphasic composition of HAp, TCP, and Whitlockite.

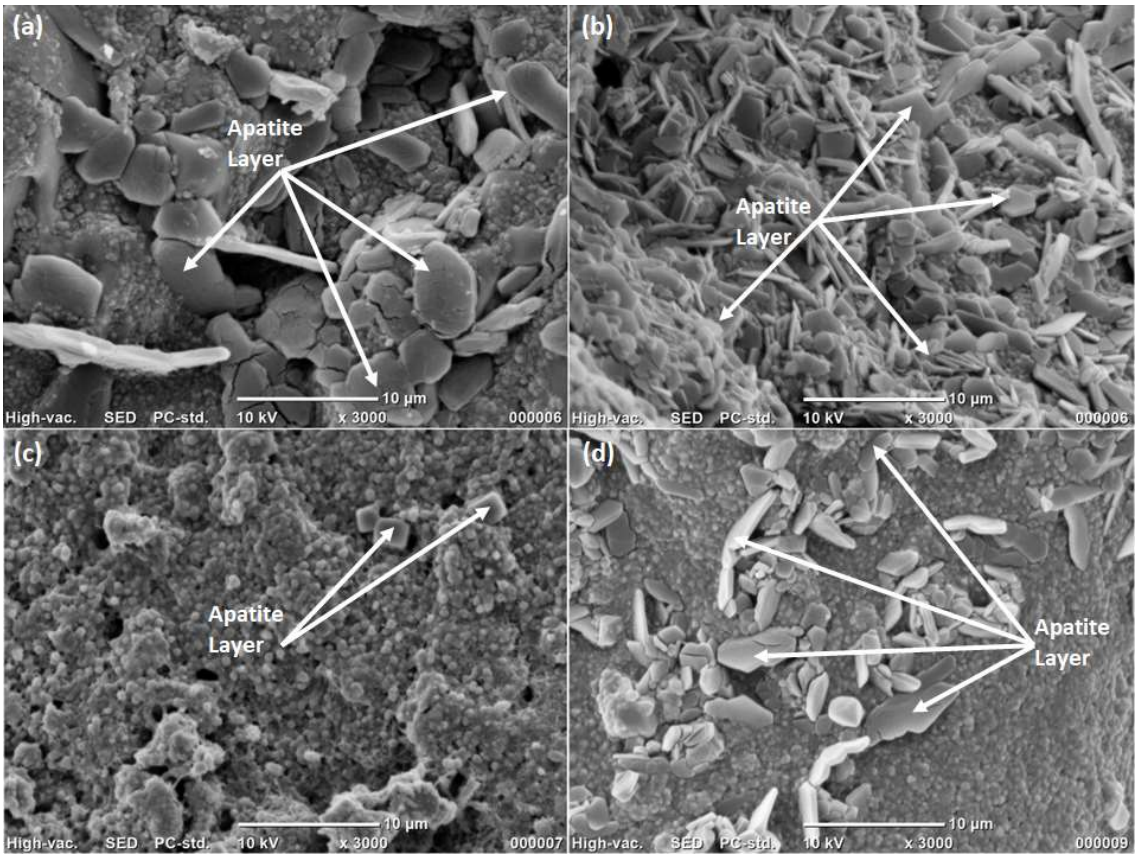

Figure. 7.11. SEM morphology shows the formation of an apatite layer on the surface of the Animal Waste Bone-Alumina toughened zirconia (AWB-ATZ) biocomposite after immersion in an SBF solution. (a) ATZ-AWB5% sample is treated at 1400°C (b) ATZ-AWB5% sample is treated at 1500°C (C) ATZ-AWB10% sample is treated at 1400°C (b) ATZ-AWB10% sample is treated at 1500°C

The mass loss of each composite following immersion in SBF is also analyzed. The pure ATZ composite exhibited minimal mass loss as the soaking time increased, with a slight increase in mass observed after 14 days, corresponding to the deposition of apatite on the ATZ composite during this period. In contrast, the AWB-doped composites displayed mass loss upon soaking, with the degree of weight loss escalating in conjunction with both the AWB content and soaking duration. Furthermore, the mass loss rate of Animal Waste Bone-Alumina toughened zirconia (ATZ-AWB) composites exhibited rapid acceleration within the initial 7 days, followed by a gradual deceleration. Corroborating this temporal trend, surface morphology analysis of the composites during this period revealed relatively limited apatite deposition. Consequently, the degradation rate of HAp, TCP, and

Whitlockite exceeded the apatite generation rate, resulting in pronounced mass loss. However, after a 14-day immersion period, a substantial amount of apatite had formed on the composite surface, compensating for the loss incurred through partial mass degradation. As a result, the mass loss rate diminished after 7 days. In summary, the composites experienced degradation when subjected to SBF immersion, exhibiting greater mass loss with increasing AWB content and soaking time. Nevertheless, the deposition of apatite after 7 days served to offset a portion of the mass loss.

7.3.5 Physical and Mechanical Characterization of Animal Waste Bone-Alumina toughened zirconia (ATZ-AWB) Biocomposite

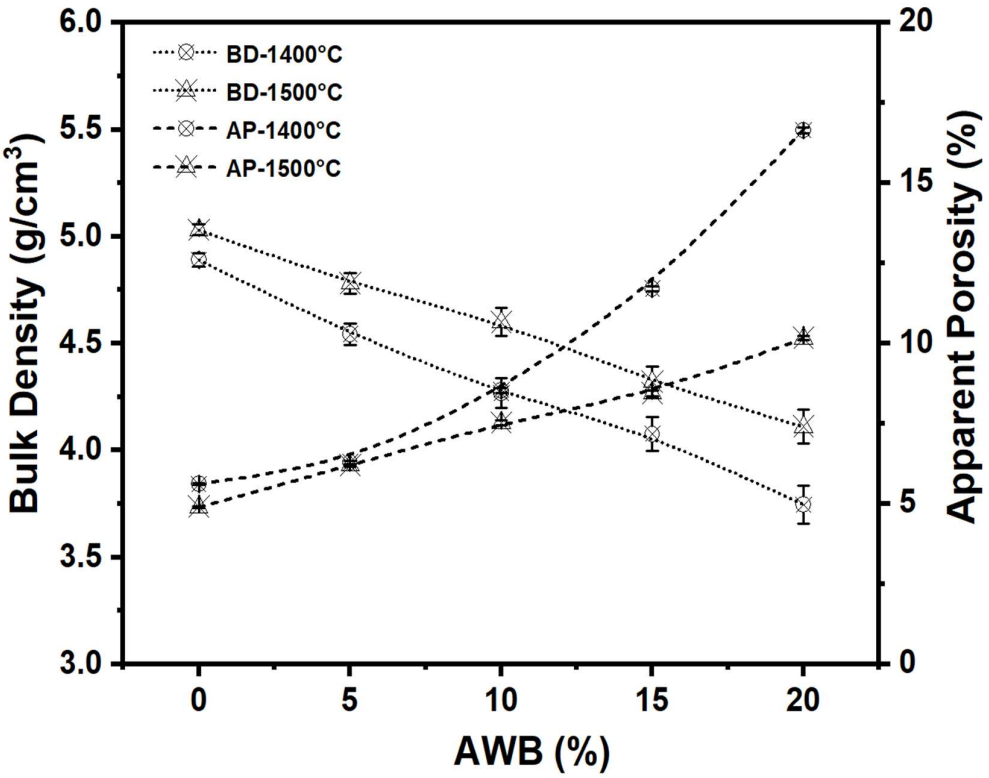

Figure. 7.12. Bulk Density and Apparent porosity variation of Alumina toughened zirconia-Animal Waste Bone (ATZ-AWB) biocomposite with AWB content.

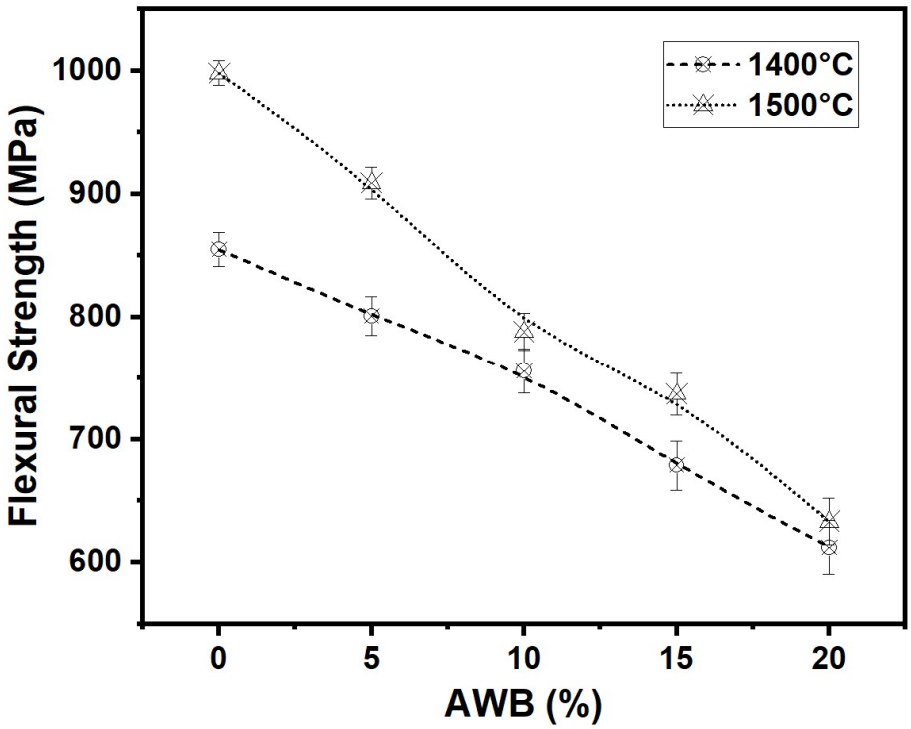

Figure. 7.13. Flexural strength variation of Alumina toughened zirconia-Animal Waste Bone (ATZ-AWB) biocomposite with AWB content.

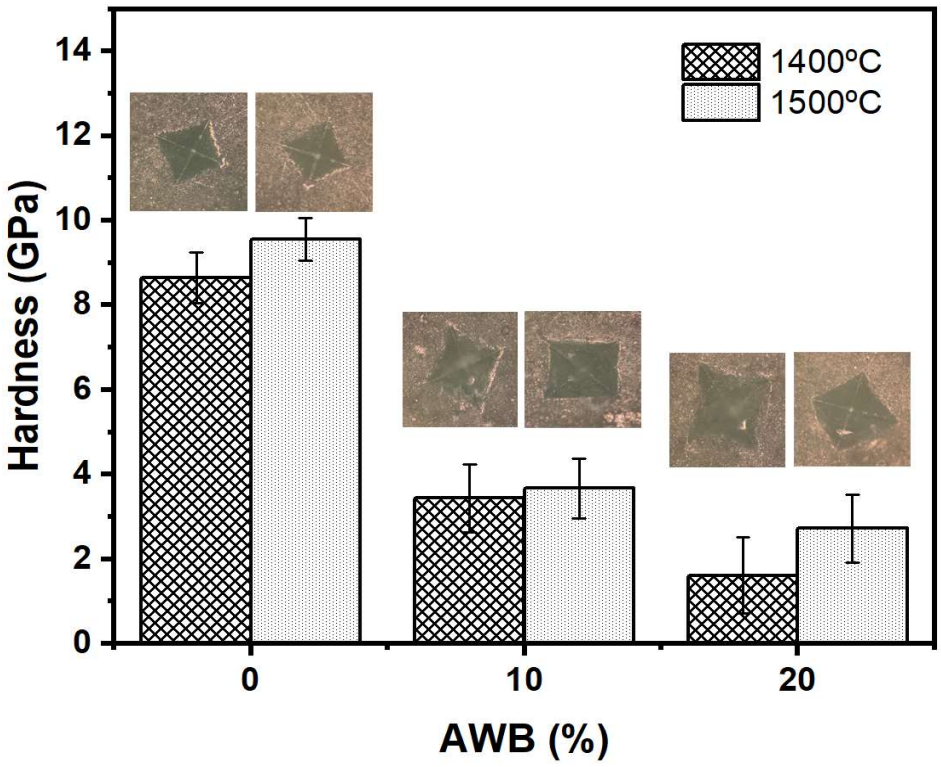

Figure. 7.14. Hardness variation of Alumina toughened zirconia-Animal Waste Bone (ATZ-AWB) biocomposite with Animal Waste Bone (AWB) content.

The physical and mechanical characteristics of the ATZ biocomposite undergo significant alterations by introducing triphasic calcium phosphate derived from AWB doping. Figure 7.12 illustrates the impact of AWB content on the bulk density and porosity of the composite after sintering at distinct temperatures (1400°C and 1500°C). It is evident that within the temperature range of 1400°C to 1500°C, the influence of AWB content on apparent porosity is directly proportional. As the AWB weight percentage increases from 0 to 20 wt%, the apparent porosity rises from 3.5% to 18%. Conversely, an inverse relationship is observed in the case of bulk density for samples sintered at the same temperatures. The decrease in density caused by AWB addition can be explained by the incorporation of lower-density HAp/TCP/Wk into the higher-density Zirconia-Alumina composite, resulting in a reduction in density for the ATZ-AWB composite as the AWB content increases. Another reason for the lower density could be attributed to a slower consolidation rate of zirconia and alumina particles due to the addition of HAp, TCP, and whitlockite, as evidenced by the apparent porosity graph, which displays an increasing trend with increasing AWB content. The lower consolidation of particle mixtures can be attributed to the distinct properties and sintering temperatures borne by each particle. The mechanical properties of the ATZ-AWB composite exhibit a direct correlation with the density and apparent porosity results. The introduction of AWB into ATZ significantly impacts the mechanical properties of the ATZ-AWB composites. The flexural strength of the composite undergoes a drastic decrease from 1000 MPa to 630 MPa as the AWB content increases from 0% to 20% (Figure.7.13). This decrease in flexural strength follows a linear trend. Samples sintered at higher temperatures display superior flexural strength measurements for a specific AWB content. Similar to the trend observed in the flexural data, the hardness value exhibits a similar pattern. The hardness of the ATZ-AWB composite decreases from 9 GPa to 2 GPa as the AWB content increases from 0% to 20%

(Fig.7.14). Samples sintered at higher temperatures demonstrate improved resistance to indentation. The decrease in flexural and hardness values with increased AWB content can be attributed to the lower mechanical properties exhibited by HAp/TCP/Wk. Although the flexural and hardness values of the composite decrease with the addition of AWB, the strength requirements for the ATZ-AWB composite, as indicated by the flexural and hardness graph, remain within the acceptable range for load-bearing applications in biomaterials. Therefore, the decrease in mechanical properties can be tolerated due to the advantage of increased bioactivity provided by AWB addition, rendering the composite suitable for bio applications.

7.4 Conclusion

In summary,

1. The bioactivity of a biocomposite based on ATZ has been significantly improved by incorporating AWB as a dopant, reducing processing costs.

2. The abundance of calcium and phosphorus elements in AWB promotes the formation of calcium phosphate phases within the composite.

3. A precise thermal treatment process is employed to consolidate the ATZ particles and induce the formation of various calcium phosphate phases (HAp/TCP/Wk), thereby enhancing the biocompatibility, osteoconduction, and osteointegration properties of the ATZ composite.

4. Magnesium's small yet significant presence in AWB facilitates the conversion of the Whitlockite phase, a primary constituent found in human bone.

5. The XRD results revealed that AWB converts to HAp, which partially decomposes

to TCP phases. With the increase in AWB concentration, these phases (HAp, TCP, and Wk) are more evident with a small portion of CaZrO3, which comes out due to a reaction between decomposed CaO from HAp and Zirconia. Transformation of tetragonal Zirconia to cubic and tetragonal forms is also favored by HAp decomposition.

6. The FTIR data also supports the XRD results, confirming the presence of triphasic calcium phosphate in the form of HAp, TCP, and Wk, along with Alumina and Zirconia phases.

7. In vitro proof-of-concept results have demonstrated that the incorporation of AWB leads to an increased formation of an apatite layer, confirming the enhanced bioactivity of the composite.

8. Including triphasic structures in HAp, TCP, and Whitlockite confers superior biological properties to the biocomposite compared to a single-phase monolith.

9. This study reveals that AWB is a promising "waste-to-resource" raw material suitable for bone graft substitutes in bone repair and regeneration.

10. Furthermore, the use of ATZ as the main matrix imparts sufficient mechanical strength to the biocomposite for load-bearing applications. The AWB-ATZ biocomposite exhibits bulk density, apparent porosity, hardness, and bending strength within the ranges of 3.7-5.2 g/cm^3, 3.6-17%, 2-9 GPa and 620-1000 MPa, respectively.

11. In terms of bioactivity (due to the presence of triphasic calcium phosphate-HAp/TCP/Wk) and cost-effectiveness, the present ATZ-AWB biocomposite

surpasses zirconia-based biocomposites doped with synthetic materials.

12. Altogether, the utilization of AWB not only amplifies bioactivity but also curtails the expenses associated with zirconia-based biomaterials, thus fortifying the principles of biocircularity and bioeconomy through a truly sustainable approach.

References

[1] B. Okumu, A.G. Kehbila, P. Osano, A review of water-forest-energy-food security nexus data and assessment of studies in East Africa, Curr. Res. Environ. Sustain. 3 (2021) 100045. https://doi.org/10.1016/j.crsust.2021.100045.

[2] M.K. Yadav, V. Pandey, K. Mohanta, V.K. Singh, A low-cost approach to develop silica doped Tricalcium Phosphate (TCP) scaffold by valorizing animal bone waste and rice husk for tissue engineering applications, Ceram. Int. 48 (2022) 25335–25345. https://doi.org/10.1016/j.ceramint.2022.05.207.

[3] M. Boutinguiza, J. Pou, R. Comesaña, F. Lusquiños, A. De Carlos, B. León, Biological hydroxyapatite obtained from fish bones, Mater. Sci. Eng. C. 32 (2012) 478–486. https://doi.org/10.1016/j.msec.2011.11.021.

[4] S. Ghosh, K. Pramanik, Unveiling the secrets of food waste-derived biomaterials in remediation of environmental pollutants – A review, Bioresour. Technol. Reports. 22 (2023) 101469. https://doi.org/10.1016/j.biteb.2023.101469.

[5] W. Russ, R. Meyer-Pittroff, Utilizing Waste Products from the Food Production and Processing Industries, Crit. Rev. Food Sci. Nutr. 44 (2004) 57–62. https://doi.org/10.1080/10408690490263783.

[6] J.K. Wang, Ç. Çimenoğlu, N.M.J. Cheam, X. Hu, C.Y. Tay, Sustainable aquaculture side-streams derived hybrid biocomposite for bone tissue engineering, Mater. Sci. Eng. C. 126 (2021). https://doi.org/10.1016/j.msec.2021.112104.

[7] E. Santolini, M. Bovo, A. Barbaresi, D. Torreggiani, P. Tassinari, Turning agricultural wastes into biomaterials: Assessing the sustainability of scenarios of circular valorization of corn cob in a life-cycle perspective, Appl. Sci. 11 (2021). https://doi.org/10.3390/app11146281.

[8] N.M. Holden, A.M. Neill, J.C. Stout, D. O'Brien, M.A. Morris, Biocircularity: a Framework to Define Sustainable, Circular Bioeconomy, Circ. Econ. Sustain. (2022) 77–

91. https://doi.org/10.1007/s43615-022-00180-y.

[9] Q. Zhu, Z. Ablikim, T. Chen, Q. Cai, J. Xia, D. Jiang, S. Wang, The preparation and characterization of HA/β-TCP biphasic ceramics from fish bones, Ceram. Int. 43 (2017) 12213–12220. https://doi.org/10.1016/j.ceramint.2017.06.082.

[10] T.F. Adepoju, M.A. Ibeh, A.J. Asuquo, Elucidate three novel catalysts synthesized from animal bones for the production of biodiesel from ternary non-edible and edible oil blend: A case of Jatropha curcus, Hevea brasiliensis, and Elaeis guineensis oil, South African J. Chem. Eng. 36 (2021) 58–73. https://doi.org/10.1016/j.sajce.2021.01.002.

[11] Y.H. Tan, M.O. Abdullah, J. Kansedo, N.M. Mubarak, Y.S. Chan, C. Nolasco-Hipolito, Biodiesel production from used cooking oil using green solid catalyst derived from calcined fusion waste chicken and fish bones, Renew. Energy. 139 (2019) 696–706. https://doi.org/10.1016/j.renene.2019.02.110.

[12] M. AlSharifi, H. Znad, Transesterification of waste canola oil by lithium/zinc composite supported on waste chicken bone as an effective catalyst, Renew. Energy. 151 (2020) 740–749. https://doi.org/10.1016/j.renene.2019.11.071.

[13] H. Mahmood Khan, T. Iqbal, C. Haider Ali, A. Javaid, I. Iqbal Cheema, Sustainable biodiesel production from waste cooking oil utilizing waste ostrich (Struthio camelus) bones derived heterogeneous catalyst, Fuel. 277 (2020) 118091. https://doi.org/10.1016/j.fuel.2020.118091.

[14] C. Chingakham, C. Tiwary, V. Sajith, Waste Animal Bone as a Novel Layered Heterogeneous Catalyst for the Transesterification of Biodiesel, Catal. Letters. 149 (2019) 1100–1110. https://doi.org/10.1007/s10562-019-02696-9.

[15] D. Prabu, P.S. Kumar, B.S. Rathi, S. Sathish, K.V. Anand, J.A. Kumar, O.B. Mohammed, P. Silambarasan, Feasibility of magnetic nano adsorbent impregnated with activated carbon from animal bone waste: Application for the chromium (VI) removal, Environ. Res. 203 (2022) 111813. https://doi.org/10.1016/j.envres.2021.111813.

[16] M.J. Amiri, A. Faraji, M. Azizi, B.G. Nejad, M. Arshadi, Recycling bone waste and cobalt-wastewater into a highly stable and efficient activator of peroxymonosulfate for dye and HEPES degradation, Process Saf. Environ. Prot. 147 (2021) 626–641. https://doi.org/10.1016/j.psep.2020.12.039.

[17] K. Jayathilakan, K. Sultana, K. Radhakrishna, A.S. Bawa, Utilization of byproducts and waste materials from meat, poultry and fish processing industries: A review, J. Food Sci. Technol. 49 (2012) 278–293. https://doi.org/10.1007/s13197-011-0290-7.

[18] N.S. El-Gendy, R.A. El-Salamony, S.A. Younis, Green synthesis of fluorapatite from

waste animal bones and the photo-catalytic degradation activity of a new ZnO/green biocatalyst nano-composite for removal of chlorophenols, J. Water Process Eng. 12 (2016) 8–19. https://doi.org/10.1016/j.jwpe.2016.05.007.

[19] G. Chakrapani, M. Zare, S. Ramakrishna, Biomaterials from the value-added food wastes, Bioresour. Technol. Reports. 19 (2022) 101181. https://doi.org/10.1016/j.biteb.2022.101181.

[20] E.A. Ofudje, A. Rajendran, A.I. Adeogun, M.A. Idowu, S.O. Kareem, D.K. Pattanayak, Synthesis of organic derived hydroxyapatite scaffold from pig bone waste for tissue engineering applications, Adv. Powder Technol. 29 (2018) 1–8. https://doi.org/10.1016/j.apt.2017.09.008.

[21] A. Niakan, S. Ramesh, P. Ganesan, C.Y. Tan, J. Purbolaksono, H. Chandran, S. Ramesh, W.D. Teng, Sintering behaviour of natural porous hydroxyapatite derived from bovine bone, Ceram. Int. 41 (2015) 3024–3029. https://doi.org/10.1016/j.ceramint.2014.10.138.

[22] M. Figueiredo, A. Fernando, G. Martins, J. Freitas, F. Judas, H. Figueiredo, Effect of the calcination temperature on the composition and microstructure of hydroxyapatite derived from human and animal bone, Ceram. Int. 36 (2010) 2383–2393. https://doi.org/10.1016/j.ceramint.2010.07.016.

[23] C. Shuai, W. Yang, P. Feng, S. Peng, H. Pan, Accelerated degradation of HAP/PLLA bone scaffold by PGA blending facilitates bioactivity and osteoconductivity, Bioact. Mater. 6 (2021) 490–502. https://doi.org/10.1016/j.bioactmat.2020.09.001.

[24] P. Feng, P. Wu, C. Gao, Y. Yang, W. Guo, W. Yang, C. Shuai, A Multimaterial Scaffold With Tunable Properties: Toward Bone Tissue Repair, Adv. Sci. 5 (2018) 1–15. https://doi.org/10.1002/advs.201700817.

[25] C. Kim, J.W. Lee, J.H. Heo, C. Park, D.-H. Kim, G.S. Yi, H.C. Kang, H.S. Jung, H. Shin, J.H. Lee, Natural bone-mimicking nanopore-incorporated hydroxyapatite scaffolds for enhanced bone tissue regeneration, Biomater. Res. 26 (2022) 7. https://doi.org/10.1186/s40824-022-00253-x.

[26] J.H. Luna-Domínguez, H. Téllez-Jiménez, H. Hernández-Cocoletzi, M. García-Hernández, J.A. Melo-Banda, H. Nygren, Development and in vivo response of hydroxyapatite/whitlockite from chicken bones as bone substitute using a chitosan membrane for guided bone regeneration, Ceram. Int. 44 (2018) 22583–22591. https://doi.org/10.1016/j.ceramint.2018.09.032.

[27] A. Yücel, S. Sezer, E. Birhanlı, T. Ekinci, E. Yalman, T. Depci, Synthesis and

characterization of whitlockite from sea urchin skeleton and investigation of antibacterial activity, Ceram. Int. 47 (2021) 626–633. https://doi.org/10.1016/j.ceramint.2020.08.170.
[28] F. Nigar, A.-L. Johnston, J. Smith, W. Oakley, M.T. Islam, R. Felfel, D. Grant, E. Lester, I. Ahmed, Production of Nano Hydroxyapatite and Mg-Whitlockite from Biowaste-Derived products via Continuous Flow Hydrothermal Synthesis: A Step towards Circular Economy, Materials (Basel). 16 (2023) 2138. https://doi.org/10.3390/ma16062138.
[29] H. Cheng, R. Chabok, X. Guan, A. Chawla, Y. Li, A. Khademhosseini, H.L. Jang, Synergistic interplay between the two major bone minerals, hydroxyapatite and whitlockite nanoparticles, for osteogenic differentiation of mesenchymal stem cells, Acta Biomater. 69 (2018) 342–351. https://doi.org/10.1016/j.actbio.2018.01.016.
[30] H.L. Jang, G. Bin Zheng, J. Park, H.D. Kim, H.R. Baek, H.K. Lee, K. Lee, H.N. Han, C.K. Lee, N.S. Hwang, J.H. Lee, K.T. Nam, In Vitro and In Vivo Evaluation of Whitlockite Biocompatibility: Comparative Study with Hydroxyapatite and β-Tricalcium Phosphate, Adv. Healthc. Mater. 5 (2016) 128–136. https://doi.org/10.1002/adhm.201400824.
[31] S.F. Ou, S.Y. Chiou, K.L. Ou, Phase transformation on hydroxyapatite decomposition, Ceram. Int. 39 (2013) 3809–3816. https://doi.org/10.1016/j.ceramint.2012.10.221.
[32] M. Frasnelli, V.M. Sglavo, Effect of Mg2+ doping on beta-alpha phase transition in tricalcium phosphate (TCP) bioceramics, Acta Biomater. 33 (2016) 283–289. https://doi.org/10.1016/j.actbio.2016.01.015.
[33] M. Inuzuka, S. Nakamura, S. Kishi, K. Yoshida, K. Hashimoto, Y. Toda, K. Yamashita, Hydroxyapatite-doped zirconia for preparation of biomedical composite ceramics, Solid State Ionics. 172 (2004) 509–513. https://doi.org/10.1016/j.ssi.2004.01.054.
[34] I. Khahtan Sabree, O. Saleh Mahdi, Characterization of Zirconia-Hydroxyapatite Nanocomposites for Orthopedic and Dental Applications, Int. J. Eng. Technol. 7 (2018) 926. https://doi.org/10.14419/ijet.v7i4.19.28072.
[35] T.J. Matsumato, S.H. An, T. Ishimoto, T. Nakano, T. Matsumoto, S. Imazato, Zirconia-hydroxyapatite composite material with micro porous structure, Dent. Mater. 27 (2011) e205–e212. https://doi.org/10.1016/j.dental.2011.07.009.
[36] J. Zhang, D. Huang, S. Liu, X. Dong, Y. Li, H. Zhang, Z. Yang, Q. Su, W. Huang, W. Zheng, W. Zhou, Zirconia toughened hydroxyapatite biocomposite formed by a DLP 3D printing process for potential bone tissue engineering, Mater. Sci. Eng. C. 105 (2019). https://doi.org/10.1016/j.msec.2019.110054.
[37] E.T.P. Bergamo, K.B. Cardoso, L.F.O. Lino, T.M.B. Campos, K.N. Monteiro, P.F.

Cesar, L.A. Genova, G.P. Thim, P.G. Coelho, E.A. Bonfante, Alumina-toughened zirconia for dental applications: Physicochemical, mechanical, optical, and residual stress characterization after artificial aging, J. Biomed. Mater. Res. - Part B Appl. Biomater. 109 (2021) 1135–1144. https://doi.org/10.1002/jbm.b.34776.

[38] G. Schierano, F. Mussano, M.G. Faga, G. Menicucci, C. Manzella, C. Sabione, T. Genova, M.M. Von Degerfeld, B. Peirone, A. Cassenti, P. Cassoni, S. Carossa, An alumina toughened zirconia composite for dental implant application: In vivo animal results, Biomed Res. Int. 2015 (2015). https://doi.org/10.1155/2015/157360.

[39] N.L. Bragazzi, R. Gasparini, D. Amicizia, D. Panatto, C. Larosa, Porous Alumina as a Promising Biomaterial for Public Health, 1st ed., Elsevier Inc., 2015. https://doi.org/10.1016/bs.apcsb.2015.08.003.

[40] J. Chevalier, L. Gremillard, Zirconia as a biomaterial, Compr. Biomater. II. 1 (2017) 122–144. https://doi.org/10.1016/B978-0-12-803581-8.10245-0.

[41] J. Fan, Y. Yuan, J. Li, J. Liu, K. Zhao, D. Liu, L. An, Densification and grain growth in oscillatory pressure sintering of alumina toughened zirconia ceramic composites, J. Alloys Compd. 845 (2020) 155644. https://doi.org/10.1016/j.jallcom.2020.155644.

[42] A.K. Pandey, U.R. Jena, K. Biswas, In vitro ageing and wear behaviour of ceria stabilized zirconia toughened alumina (CSZ-TA) bio-ceramic, Mater. Chem. Phys. 146 (2014) 456–463. https://doi.org/10.1016/j.matchemphys.2014.03.053.

[43] M.G. Faga, A. Vallée, A. Bellosi, M. Mazzocchi, N.N. Thinh, G. Martra, S. Coluccia, Chemical treatment on alumina-zirconia composites inducing apatite formation with maintained mechanical properties, J. Eur. Ceram. Soc. 32 (2012) 2113–2120. https://doi.org/10.1016/j.jeurceramsoc.2011.12.020.

[44] Y.M. Kong, C.J. Bae, S.H. Lee, H.W. Kim, H.E. Kim, Improvement in biocompatibility of ZrO_2-Al2O3 nano-composite by addition of HA, Biomaterials. 26 (2005) 509–517. https://doi.org/10.1016/j.biomaterials.2004.02.061.

[45] P. Nandha Kumar, S. Kannan, Quantitative analysis of the structural stability and degradation ability of hydroxyapatite and zirconia composites synthesized in situ, RSC Adv. 4 (2014) 29946–29956. https://doi.org/10.1039/c4ra02441a.

[46] S. Batool, U. Liaqat, Z. Hussain, M. Sohail, Synthesis, characterization and process optimization of bone whitlockite, Nanomaterials. 10 (2020) 1–14. https://doi.org/10.3390/nano10091856.

[47] H.L. Jang, K. Jin, J. Lee, Y. Kim, S.H. Nahm, K.S. Hong, K.T. Nam, Revisiting Whitlockite, the Second Most Abundant Biomineral in Bone: Nanocrystal Synthesis in

Physiologically Relevant Conditions and Biocompatibility Evaluation, ACS Nano. 8 (2014) 634–641. https://doi.org/10.1021/nn405246h.

[48] K. Prem Ananth, S. Shanmugam, S.P. Jose, A. Joseph Nathanael, T.H. Oh, D. Mangalaraj, A.M. Ballamurugan, Structural and chemical analysis of silica-doped β-TCP ceramic coatings on surgical grade 316L SS for possible biomedical application, J. Asian Ceram. Soc. 3 (2015) 317–324. https://doi.org/10.1016/j.jascer.2015.06.004.